ADVANCED ENERGY & SUSTAINABILITY RESEARCH
www.advenergysustres.com

Enhanced and Durable Light-Driven Hydrogen Evolution by Cobalt-Based Prussian Blue Analogs in Phospholipid Bilayers

*Subrata Mandal, Akash Deshpande, Robert Leiter, Johannes Biskupek, Ute Kaiser, and Andrea Pannwitz**

Light-driven hydrogen (H_2) evolution in water is performed using a series of cobalt-based Prussian blue analogs (M—Co PBAs) with $M^{II}{}_3[Co^{III}(CN)_6]_2$, M = Co, Ni, Cu, Zn embedded in phospholipid bilayers with the amphiphilic ruthenium-based photosensitizer RuC_9. Hydrophobic surface functionalization of M—Co PBA nanoparticles with oleylamine facilitates close proximity of the PBA to the photosensitizer within lipid bilayers of vesicles, enhancing photocatalytic performance. The type of metal and rigidity of the lipid environment significantly influences hydrogen evolution reaction efficiency, with the trend: Ni > Co > Zn > Cu and DMPC > DOPC > DPPC. Among these, Ni—Co PBA in DMPC: (14:0 PEG2000 PE) vesicles shows the highest efficiency, with a ninefold increase in H_2 production compared to the conventional aqueous system. This sustained activity is attributed to the efficient electron transfer and the scaffold's stability. This study provides valuable insights for the development of scalable and cost-effective photocatalytic technologies.

1. Introduction

Producing solar fuels through photocatalytic water splitting or the hydrogen evolution reaction (HER) is recognized as an environmentally friendly and sustainable process, offering the potential to reduce our reliance on fossil fuels.[1] There is a great demand for low-cost, scalable, and efficient HER catalysts (CATs). Prussian blue analogs (PBAs) can, in principle, provide such CATs, as they are composed of the general composition $M^{II}{}_3[M'^{III}(CN)_6]_2{\cdot}nH_2O$, with M and M' being earth-abundant and usually cheap metals, straightforward synthesis, and outstanding chemical stability across a wide range of pH levels. However, despite the porosity of these 3D coordination compounds, their high crystallinity limits the number of surface-active and catalytically active sites. It hinders efficient electron transfer with molecular species such as electron donors and molecular photosensitizers (PS). One approach to enhance the number of catalytically active sites is to increase the number of defects in the structure. Intrinsic defect sites caused by the loss of $[M^{III}(CN)_6]^{2-}$ units allow M^{II} cations to serve as active sites for catalysis.[2–5] For example, the Yamada group achieved substantial enhancement in photocatalytic water oxidation activity at pH 7 and in the presence of the $[Ru(bpy)_3]^{2+}$ (bpy = 2,2′-bipyridine) as a PS and $Na_2S_2O_8$ as an electron acceptor by introducing a small amount of Ca^{2+} ions into a polymeric cobalt cyanide structure, forming $Ca_x[Co^{II}(H_2O)_2]_{1.5-x}[Co^{III}(CN)_6]$.[6] In another approach, the Ding group varied the divalent metal ions (M^{II} = Mn, Fe, Co, Ni, Cu) to improve photocatalytic CO_2 reduction, producing

S. Mandal, A. Deshpande, A. Pannwitz
Institut für Anorganische Chemie I
Universität Ulm
Albert-Einstein-Allee 11, 89081 Ulm, Germany
E-mail: Andrea.pannwitz@uni-jena.de

R. Leiter, J. Biskupek, U. Kaiser
Central Facility of Electron Microscopy
Electron Microscopy Group of Material Science
University of Ulm
Albert-Einstein-Allee 11, 89081 Ulm, Germany

The ORCID identification number(s) for the author(s) of this article can be found under https://doi.org/10.1002/aesr.202400372.

DOI: 10.1002/aesr.202400372

A. Pannwitz
Institut für Anorganische und Analytische Chemie
Friedrich-Schiller-Universität Jena
Humboldtstr. 8, 07743 Jena, Germany

A. Pannwitz
Center for Energy and Environmental Chemistry Jena (CEEC)
Friedrich-Schiller-Universität Jena
Philosophenweg 7a, 07743 Jena, Germany

A. Pannwitz
Helmholtz Institute for Polymers in Energy Applications Jena (HIPOLE Jena)
Lessingstraße 12–14, 07743 Jena, Germany

CO in the presence of $[Ru(bpy)_3]^{2+}$ and triethanolamine (TEOA) in an H_2O/CH_3CN mixture.[2] However, in all reported studies, undesirable degradation of the Ru-based PS occurred by the loss of bpy ligands, limiting the applicability of the reported photocatalytic systems with PBAs. In most cases, the decomposition of the PS is faster than electron transfer with the PBA active sites because of the limited active site availability of the heterogeneous PBA material.[4,7–9]

In this study, we increased the surface area and number of accessible active sites by downsizing the bulk structure to produce nanoparticles. The nanoparticles are stabilized by the introduction of long alkyl chains on the surface.[10] While this strategy effectively enhances the structural attributes of the particles, it simultaneously introduces significant hydrophobicity. While this hydrophobic coverage is anticipated to have negative consequences on electron transfer between water-soluble $[Ru(bpy)_3]^{2+}$ and the poorly water-soluble PBA in water, the coassembly with amphiphilic lipid bilayers and an amphiphilic PS might be advantageous and was performed herein.

Phospholipid bilayers (**Figure 1**) are formed in water from phospholipids. They build up vesicles such as liposomes (typically < 1000 nm) or giant vesicles (>1000 nm), which can provide a sophisticated and bioinspired framework for photocatalysis.[11–13] Depending on their charge and hydrophobic or amphiphilic nature, PS and CAT molecules as well as sacrificial agents can be self-assembled in or at these lipid bilayers.[11] Crucially, these nanomembranes create a water–lipid bilayer interface at the nanoscale, enabling hydrophobic components to interact with the aqueous environment. Moreover, these synthetic liposomes and vesicles enhance charge transfer due to the spatial coassembly.

In this work, we selected oleylamine (OA)-capping of $M^{II}{}_3[Co^{III}(CN)_6]_2$ nanoparticles (M—Co PBA), generating M—Co PBA@OA ($M^{II}{}_3[Co^{III}(CN)_6]_2{\cdot}n$OA). To investigate the best earth-abundant metal composition, we tested the divalent metal ions of M = Co, Ni, Cu, and Zn. Based on previous positive experience with catalytic light-driven water splitting and CO_2 reduction in lipid bilayers,[13–17] we chose lipids with the zwitterionic choline head groups. To investigate the influence of a more or less rigid environment, we tested the following lipids: 1,2-dimyristoyl-*sn*-glycero-3-phosphocholine 14:0 PC (DMPC, at the transition temperature T_m at room temperature), 1,2-dioleoyl-*sn*-glycero-3-phosphocholine 18:1 (Δ^9-*cis*) PC (DOPC, fluid phase at room temperature), and 1,2-dipalmitoyl-*sn*-glycero-3-phosphocholine 16:0 PC (DPPC, gel phase at room temperature). We additionally added the sterically stabilizing lipid 1,2-dimyristoyl-*sn*-glycero-3-phosphoethanolamine-*N*-[methoxy(polyethylene glycol)-2000] (14:0 PEG2000 PE). Unlike previously published work with PBA photocatalysis in water,[2,3,6] we report on the first example to embed the PBA CAT in lipid bilayer vesicles. We chose the amphiphilic PS RuC9: $[Ru(bpy)_2(C9\text{-}bpy)_2]^{2+}$ (bis(2,2′-bipyridine)-(4,4′-dinonyl-2,2′-bipyridine)-ruthenium(II)) and a mixture of sacrificial donor, tTEOA, and ascorbic acid ($AscH_2$) as electron donor for HER (see Figure 1).

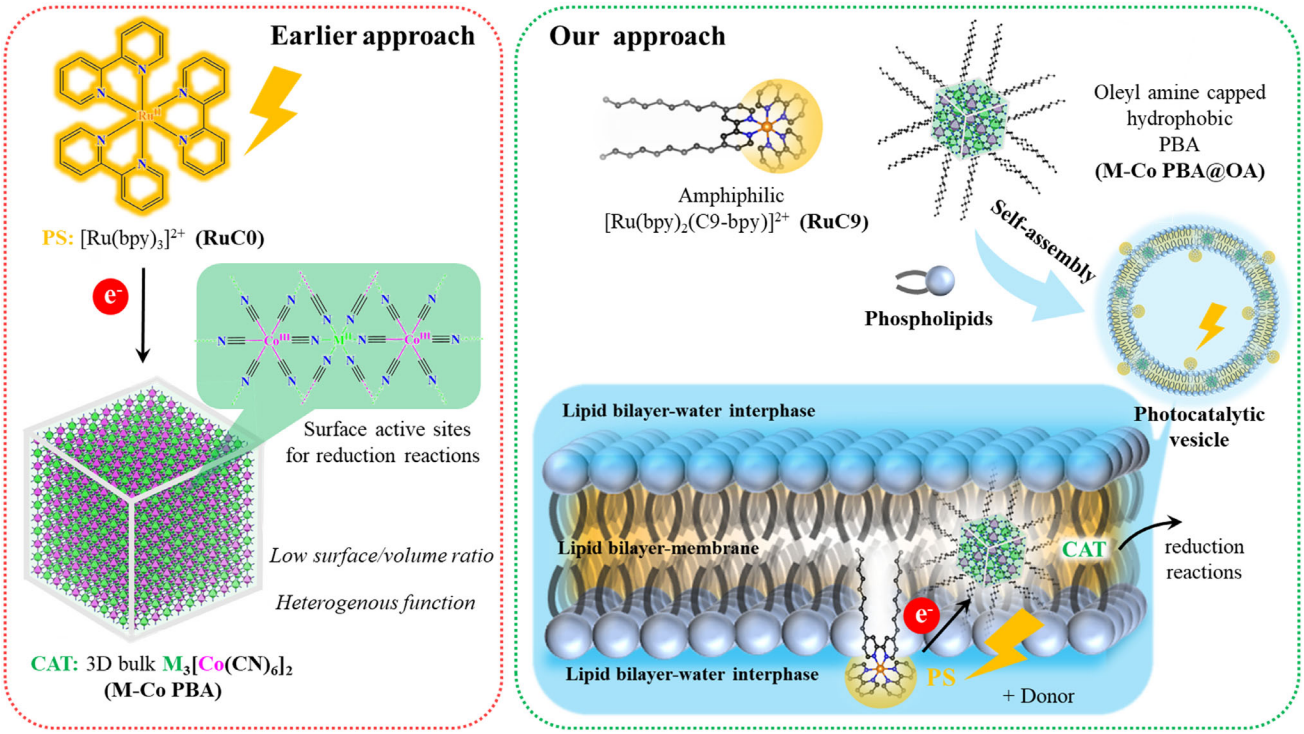

Figure 1. Schematics showing earlier heterogeneous approach (left) and our approach (right) for photocatalytic reduction reaction by integrating OA-capped hydrophobic and ultrafine M—Co PBA nanoparticles (M = Co, Ni, Cu, and Zn) as a CAT (M—Co PBA@OA) and an amphiphilic PS: $[Ru(bpy)_2(C9\text{-}bpy)]^{2+}$ (RuC9) into a bilayer of phospholipids-based vesicle.

2. Results and Discussion

2.1. Synthesis and Structural Characterization of M—Co PBA@OA (M = Co, Ni, Cu, and Zn)

To prepare the M—Co PBA bulk structure ($M^{II}_3[Co^{III}(CN)_6]_2 \cdot nH_2O$), 3 equivalents of the aq. M^{2+} precursor ($CoCl_2 \cdot 6H_2O$/$NiCl_2 \cdot 6H_2O$/$ZnCl_2 \cdot 4H_2O$/$CuSO_4 \cdot 5H_2O$) were precipitated with 2 equivalents cobalt hexacyanoferrate(III) (step 1 in **Figure 2**a, and see SI for detailed experimental and characterization). To synthesize and hydrophobically functionalize the bulk M—Co PBAs, we adapted a postsynthetic route with OA (step 2, Figure 2a). The solid products (M—Co PBA@OA) were characterized by powder X-Ray diffraction (PXRD) and attenuated total reflectance infrared (ATR-IR) spectroscopy. PXRD analysis of all bulk M—Co PBA and M—Co PBA@OA samples showed diffraction peaks at 14.77°, 17.30°, 24.56°, 35.02°, and 39.30°, corresponding to the (111), (200), (220), (400), and (420) planes. These peaks matched the simulated PDF # 89-3738 pattern, confirming that the face-centered-cubic structure remained intact and unaltered (Figure 2b and S1a, Supporting Information).

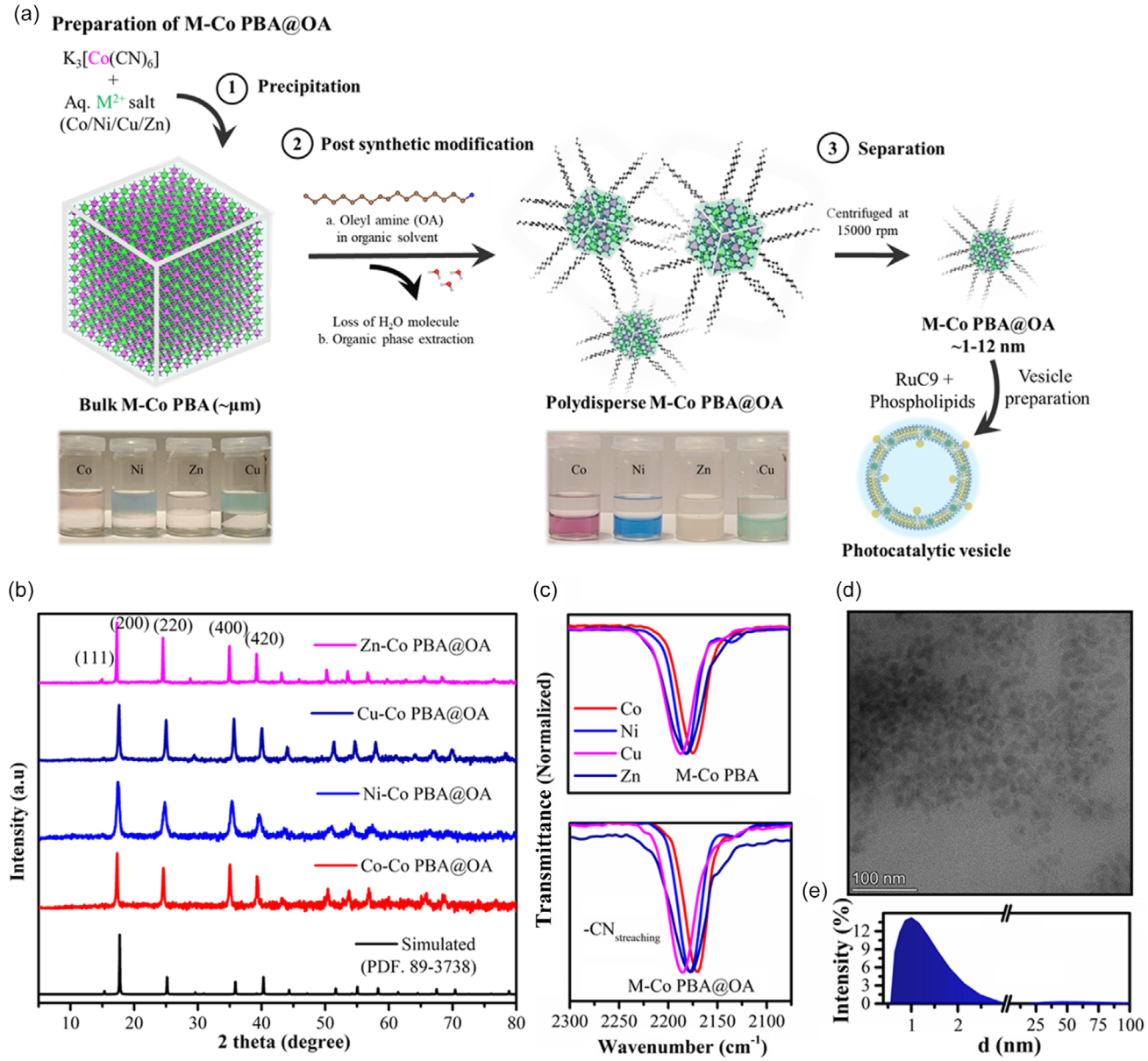

Figure 2. a) Steps (1–3) involved to synthesize and isolate OA-capped hydrophobic and ultrafine M—Co PBA nanoparticles (M—Co PBA@OA) prior to coassembling it into the vesicle bilayer along with the RuC9-based PS. Photograph showing characters of PBA particles in $H_2O/CHCl_3$ biphasic layer before and after functionalization. The insoluble PBAs are transformed into $CHCl_3$ dispersible by the surface modification. b) PXRD patterns and c) FTIR spectra in the ATR mode of OA-capped M—Co PBAs (M—Co PBA@OA, M = Co, Ni, Cu, and Zn). d) HRTEM image (scale bar 100 nm) and e) DLS particle size distribution curve of the representative Ni—Co PBA@OA isolated in $CHCl_3$ solution (the *x*-axis contains a break between 3 and 3.1 nm).

Attenuated total reflection infrared (ATR-IR) spectra show that the principal —C≡N vibration bands in all of these M—Co PBA@OA solids are located in the wavenumber range of 2170–2190 cm^{-1} (for Co at 2170 cm^{-1}, Ni and Zn at 2177 cm^{-1}, and Cu at 2177 cm^{-1}) and remain unchanged when compared to their bulk M—Co PBA structure (Figure 2c and S1b, Supporting Information). This confirms the presence of the M^{II}—N≡C—Co^{III} structure in the modified PBAs (M—Co PBA@OA). Some PBAs and their PBA@OA analogs have a weak additional —C≡N stretching region at around 2130–2140 cm^{-1}, likely due to various coordination modes within the PBA structure, potentially as a result of structural defects and possible linkage isomerism of the CN ligand or multiple valence states of the metal centers.[4,18] Upon OA capping, additional bands at 1463 cm^{-1} and in the 3300–2800 cm^{-1} appeared, corresponding to —CH_2— bending and various stretching modes (=C—H, terminal —CH_3, and methylenic C—H) of the hydrocarbon chain of the OA (see Figure S1b, Supporting Information).[19] Consequently, the M—Co PBA@OA solids exhibited higher dispersibility and stability in organic solvents compared to their bulk M—Co PBA counterparts (see Figure 2a, and S2, Supporting Information). The isolated hydrophobic M—Co PBA@OA particles in $CHCl_3$ solution (step 3, Figure 2a), obtained after removing large residues by centrifugation at 15 000 rpm, showed a typical hydrodynamic diameter (Z_{Avg}) of ≈1–12 nm according to dynamic light scattering (DLS) (Figure S3, Supporting Information). The particles of divalent Co, Ni, and Cu were relatively monodispersed, with Z_{Avg} values of ≈3.7, 1, and 7 nm, respectively, and polydispersity index (PDI) of 0.3002, 0.2196, and 0.3014. However, the Zn—Co PBA@OA particles were an exception, displaying a Z_{Avg} of 12.4 nm and a higher PDI of 0.5342 (**Table 1**). Compared to the bulk M—Co PBA (as detailed in Table S2, Supporting Information), a significant reduction in particle size was observed. ^{1}H NMR studies of the M—Co PBA@OA in $CDCl_3$ further confirmed the presence of OA in all four M—Co PBA@OA analogs, as indicated by its characteristic chemical shifts (Figure S4, Supporting Information). The OA content was estimated using nitrobenzene as an internal standard (see Supporting Information for details and Figure S5–S8, Supporting Information). This analysis also aided in calculating the coverage (n) of OA on the M—Co PBA ($M^{II}{}_3[Co^{III}(CN)_6]_2$), allowing the empirical formula of M—Co PBA@OA as $M^{II}{}_3[Co^{III}(CN)_6]_2{\cdot}n$OA to be determined in the stock solution (see detailed calculations in Supporting Information and Table S3, Supporting Information). The results presented in Table 1 indicate that the molar ratio of OA to M—Co PBA varies in M—Co OBA@OA nanoparticles, and it shows an inverse relationship between the size of the M—Co PBA@OA particles and the extent of OA (n) coverage.

The Ni—Co PBA@OA, as a representative among the synthesized M—Co PBA@OAs, was studied in detail by high-resolution transmission electron microscopy (HRTEM) which further evidenced nanoparticle (10 nm) formation, shown in Figure 2d. The aggregation and relatively larger size on the HRTEM image, compared to Z_{Avg} measured by DLS (Figure 2e), is due to solvent evaporation. Additional analysis with energy-dispersive X-Ray spectroscopy revealed a ratio of Ni/Co in Ni—Co PBA@OA to be 1.48 (see Figure S9, Supporting Information, for details), which is in good agreement with the ideal value of Ni/Co = 1.5 in a $Ni^{II}{}_3[Co^{III}(CN)_6]_2$ assembly. Along with the NMR results, the sum formula of the Ni—Co PBA@OA is $Ni^{II}{}_3[Co^{III}(CN)_6]_2{\cdot}21$ OA.

2.2. Structural Characterization of the Vesicles

Vesicles were prepared according to the methods outlined in the Experimental Section and Scheme S1, Supporting Information, using the lipid DMPC and a 14:0 PEG2000 PE at a molar ratio of 100:1. This mixture was combined with the PS: $[Ru(bpy)_2(C9\text{-}bpy)](PF_6)_2$ and M—Co PBA@OA CAT in $CHCl_3$ (step 1), followed by film formation by solvent evaporation (step 1). The resulting film was then rehydrated by an aqueous sacrificial donor solution containing 1:1 TEOA/$AscH_2$ (step 3). Following the agitation (step 4) and extrusion steps (step 5), the vesicle with the representative CAT (Ni—Co PBA@OA) was diluted (three times) and first analyzed by DLS study, which estimated their hydrodynamic diameter (Z_{Avg}) to be 122.6 nm, with a polydispersity index of 0.1983 (**Figure 3**a, and Table S4, Supporting Information). Importantly, the incorporation of the CAT did not significantly alter the size of the vesicles, as they remained consistent with those prepared using PS alone (Z_{Avg} = 121.6 nm). Furthermore, transmission electron microscopy (TEM) analysis of the light-active vesicles was performed using a negative staining technique with uranyl acetate as the contrasting agent. The representative TEM images of photocatalytically active DMPC liposomes are shown in Figure 3b,c. It shows spherical structures with a wrinkled appearance, typical for vesicles after the vacuum-drying process required for TEM analysis.[20–22] Additionally, some vesicles with relatively larger

Table 1. Structural parameters of M—Co PBA@OA and composition/concentration of $M^{II}{}_3[Co^{III}(CN)_6]_2$ and OA in their $CHCl_3$ stock solution.

PBAs	M—Co PBA@OA in $CHCl_3$		[M—Co PBA]:[OA][a]	[M—Co PBA@OA] [mM][b]	Sum formula
	Avg. size (Z_{Avg}) [nm]	Polydispersity index (PDI)			$M^{II}{}_3[Co^{III}(CN)_6]_2{\cdot}n$OA
Co—Co PBA	3.775	0.3002	1:4.6	14.6	$Co^{II}{}_3[Co^{III}(CN)_6]_2{\cdot}4.6$ OA
Ni—Co PBA	1.039	0.2196	1:21	2.4	$Ni^{II}{}_3[Co^{III}(CN)_6]_2{\cdot}21$ OA
Cu—Co PBA	6.980	0.3014	1:2.3	10.5	$Cu^{II}{}_3[Co^{III}(CN)_6]_2{\cdot}2.3$ OA
Zn—Co PBA	12.36	0.5342	1:0.5	12.00	$Zn^{II}{}_3[Co^{III}(CN)_6]_2{\cdot}0.5$ OA

[a]Molar ratio of $M^{II}{}_3[Co^{III}(CN)_6]_2$ and OA measured from ^{1}H NMR studies. [b]Concentration of the M—Co PBA@OA stock solution in 11 mL of $CHCl_3$ is based on the sum formula ($M^{II}{}_3[Co^{III}(CN)_6]_2{\cdot}n$OA).

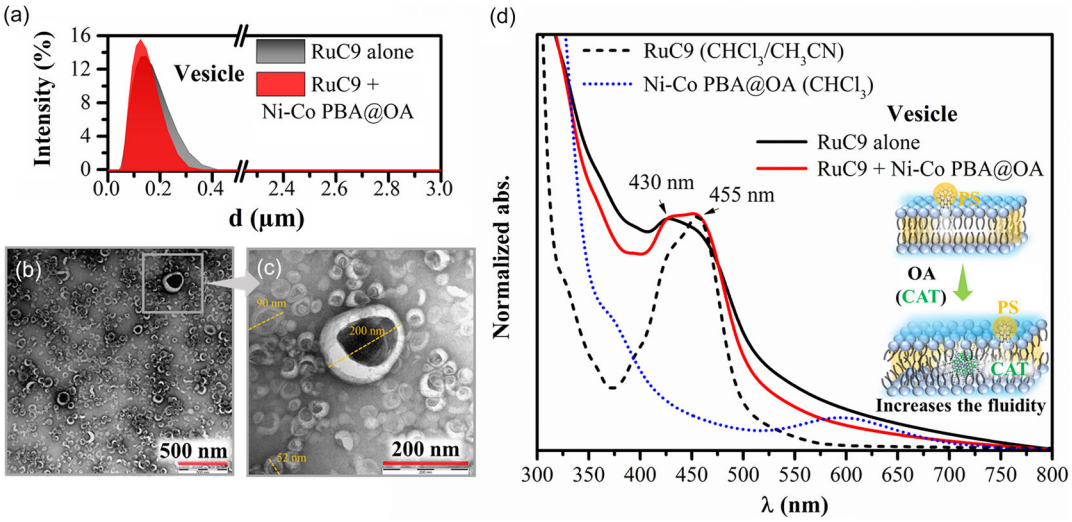

Figure 3. a) DLS particle size distribution curve of the vesicles prepared with 1) RuC9 alone and 2) the RuC9 with a representative PBA: Ni—Co PBA@OA (the *x*-axis contains a break between 0.5 and 2.25 μm). b) TEM and c) HRTEM images of negatively stained vesicle sample (2) with a composition of 100:1 DMPC: (14:0 PEG2000 PE) prepared with 17 mM of (1:1) TEOA/$AscH_2$, 55 μM of RuC9, and 10 μM of Ni—Co PBA@OA. d) Steady state and normalized UV–vis absorption spectra of the vesicles with a composition of 100:1 DMPC: (14:0 PEG2000 PE) prepared with 1) 55 μM of RuC9 alone (black and solid line) and 2) 55 μM of the RuC9 with 5 μM of Ni—Co PBA@OA (red and solid line) and a comparison with UV–vis abs spectra of the respective RuC9 (black, dashed line) and Ni—Co PBA@OA (blue and dotted line) at their solution state. The scheme (inset) demonstrates the increase in membrane fluidity upon incorporating the Ni—Co PBA@OA as a CAT.

diameters appeared to have been disrupted, likely as a result of temperature and pressure fluctuations during the TEM procedure, causing deformation of the originally spherical structures. The vesicles in TEM have a typical size below 200 nm, which is in line with the results from DLS. Overall, the TEM analysis confirmed the vesicles' size and morphology, which were consistent with the DLS results. Acquiring information on the active component within the local structure of the vesicles was still not possible from the above studies. We selected steady-state absorption and emission spectroscopy to locally characterize the vesicles. To ensure that any observed effects were solely due to the vesicles and their photocatalytic components, we prepared the vesicles without the sacrificial donor, thereby eliminating any potential interference from its presence. The UV–vis absorption spectra of the vesicles containing the PS and CAT were also compared to those of their counterparts and the PS component in a separate organic solvent matrix, as depicted in Figure 3d. This comparison allowed us to evaluate any spectral shifts or differences in absorption behavior between the vesi cle-bound PS and CAT and its isolated form. The characteristic low-energy vibrational state of the metal-to-ligand charge-transfer (MLCT)-absorption maxima at 455 nm of PS in $CH_3CN/CHCl_3$ medium undergoes a significant blue shift (25 nm) when compared to the PS in vesicle structure. The observed blue shift in the MLCT band of $[Ru(bpy)_2(C9\text{-}bpy)]^{2+}$ encapsulated within vesicles can be attributed to two main factors: 1) the distortion of the complex's octahedral geometry due to steric constraints from the rigid phospholipid bilayer environment, which alters the ligand field, indicating successful immobilization of the complex at the bilayer surface,[23,24] and 2) changes in the ground or excited states of the complex as a result of encapsulation, which modifies the electronic transitions (MLCT).[25–27] Notably, when the CAT is cointroduced with the PS into the vesicle system, a partial restoration of the MLCT band is observed, accompanied by an increase in fluorescence intensity compared to PS alone (Figure S10, Supporting Information). This effect can likely be attributed to the reduction in bilayer rigidity, caused by the surface-bound unsaturated hydrocarbon chains from the OA in the CAT.[28] These interactions could ease the steric constraints on the $[Ru(bpy)_2(C9\text{-}bpy)]^{2+}$ complex, partially restoring its octahedral geometry and thus its spectral properties.

We also used confocal optical microscopy to locate the PS and CAT within the giant vesicle. Giant vesicles typically form before the extrusion step in the vesicle preparation process (as shown in Scheme S1, Supporting Information). These vesicles are generally larger, exceeding 1 μm in size, and tend to be multilamellar, distinguishing them from smaller bilayer vesicles (such as liposomes, which are usually under 100 nm). Due to their size, giant vesicles can be readily detected using standard optical techniques, which are constrained by physical limits.[29–31] To this end, a 2-aminoanthracene (AA)-based fluorophore[32] was tagged onto Ni—Co PBA, followed by OA-modification to create a Ni—Co PBA@OA-AA analog (**Figure 4**a and see the Experimental Section for details). A similar route of vesicle preparation was followed with the PS. Large multilamellar vesicles (MLVs) were used for focusing. The optical images of these giant vesicles are shown in Figure 4b and clearly show spherical, multilamellar structures. Luminescence images acquired above 600 nm (red, Figure 4c) and at 510 nm (green, Figure 4d), excited at 488 and 405 nm, respectively, revealed ring-like structures consistent with the active units within the lipid bilayer. Emission from the $[Ru]^{2+}$ in PS and the 2-aminoanthracene tagged to CAT was observed only in the lipid environment. Although there was significant spectral overlap at high-energy

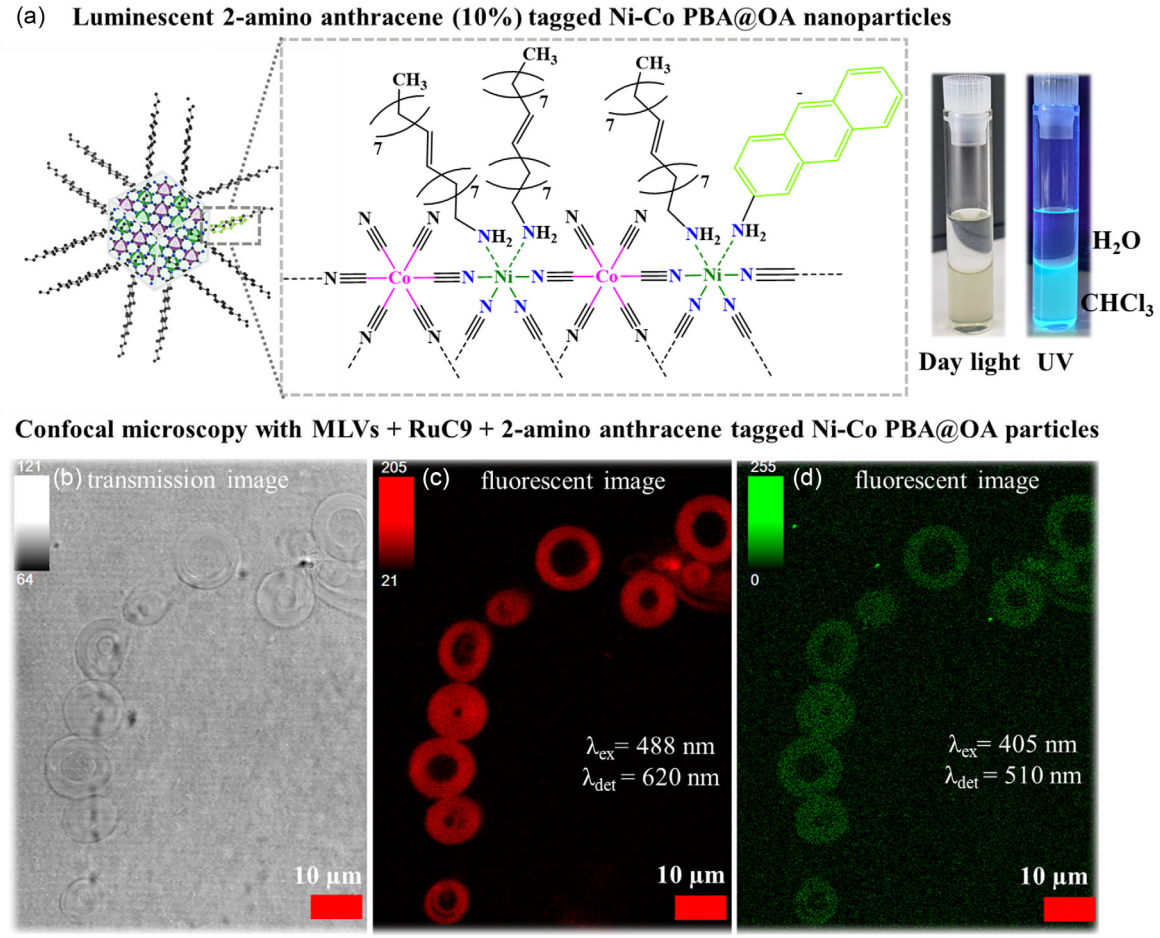

Figure 4. a) Schematic showing 10% 2-aminoanthracene tagged at the surface of Ni—Co PBA@OA nanoparticles. Photograph showing emission characteristics at the green region (510 nm) and retains similar dispersion characteristics in $H_2O/CHCl_3$ as that of nonemissive Ni—Co PBA@OA. b) Transmitted image acquired from confocal microscopy of giant MLVs embedded with a RuC9 and a green fluorophore tagged Ni—Co PBA@OA and confocal luminescence images c) at excitation = 488 nm for RuC9 with detection wavelength 620 nm and d) at excitation 405 nm for fluorophore tagged Ni—Co PBA@OA with detection wavelength of 510 nm. The MLVs were prepared with 100: 1 DMPC: (14:0 PEG2000 PE), 55 µM of RuC9, and 30 µM of Ni—Co PBA@OA.

excitation (405 nm), detection at a selective wavelength (510 nm) revealed distinct domains in the lipid environment, with the signal corresponding to the CAT tagged with the green fluorophore.

2.3. Photocatalytic Hydrogen Evolution

The HER activity of the vesicles, driven by visible light, was assessed after incorporating the active components PS, CAT, and the aqueous sacrificial electron donor into the liposomes. The photocatalytic liposomes were prepared and diluted three times with deaerated water in an Ar atmosphere (glove box). Four milliliters of this solution were transferred to an 8 mL screw cap gas chromatography (GC) vial with an airtight septum and irradiated at 460 nm using an LED source within a 3D-printed photoreactor.[20] The products were identified and quantified using GC over time (see Experimental Part and pages 12–14, Supporting Information, for more details). Initially, vesicles (DMPC: PEG (100:1) of four different M—Co PBA@OA (M = Co, Ni, Cu, and Zn) were screened with RuC9 and in the presence of [TEOA/$AscH_2$] (1:1) under the similar experimental conditions. The amount of H_2 produced (µmol) over time (h) up to 68 h for each M—Co PBA@OA is depicted in **Figure 5**a. In all cases, a steady increase in H_2 production was observed over a period exceeding 24 h. The turnover numbers (TON) of H_2, shown in **Table 2** and Figure 5a and S11a, Supporting Information, indicated that the HER activity of PBAs follows this order: Ni—Co (131) > Co—Co (69) > Zn—Co (31) > Cu—Co (2.5, 24 h). Thermodynamically, all PBAs are suitable for electron capture from the LUMO of Ru(II)-based PS and HER as they have conduction band potentials less negative than PS and more negative than −0.41 V versus NHE at pH 7.[33] However, divalent Ni(II) and Co(II) ions are more electrochemically active compared to Cu(II) and Zn(II) in PBAs,[34] making them strong candidates for enhanced HER activity. The superior reduction behavior of Ni(II), followed closely by Co(II), aligns with findings by Ding et al. in their study of bulk PBA structures for photocatalytic CO_2 reduction reactions.[2] This suggests that even after OA modification of M—Co PBAs (Ni, Co) and their

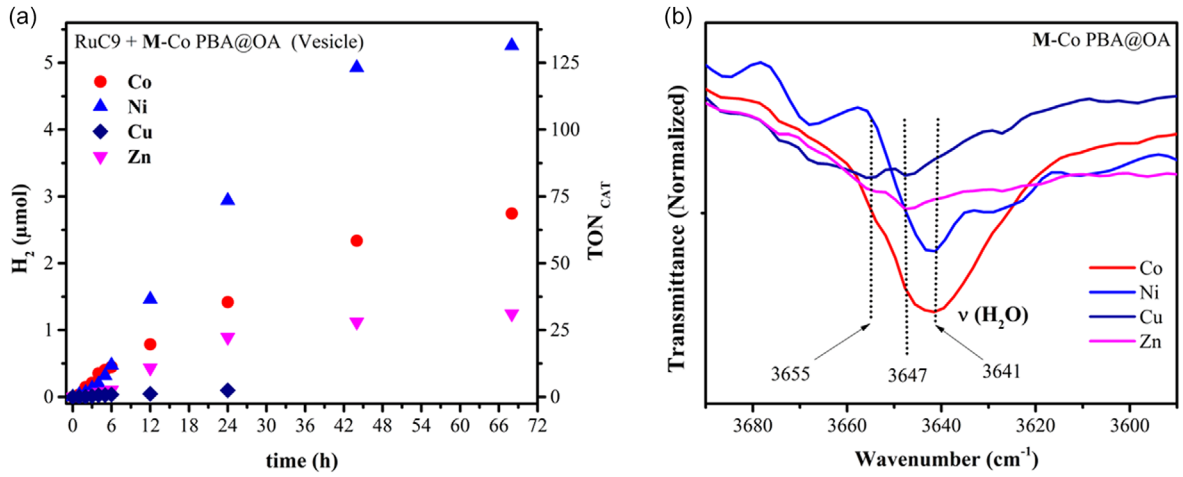

Figure 5. a) Time-dependent HER activity and TON_{CAT} results of the M—Co PBA@OA-based vesicles (M = Co, Ni, Cu, and Zn) monitored over 68 h under the following reaction conditions: [RuC9] = 55 µM, [M—Co PBA@OA] = 10 µM, light source: 460 nm LED, lipid = DMPC: (14:0 PEG2000 PE) (100:1), [TEOA/$AscH_2$] (1:1) = 17 mM and b) the high-resolution IR spectra (3590–3690 cm^{-1}) of M—Co PBA@OAs measured in the solid state.

Table 2. HER efficiency (TON_{CAT}) of the M—Co PBA@OA (M = Co, Ni, Cu, and Zn) in their prepared vesicle after 68 h of irradiation under the following reaction conditions: [RuC9] = 55 µM, [M—Co PBA@OA] = 10 µM, light source: 460 nm LED, lipid = DMPC: PEG (100:1), [TEOA/$AscH_2$] (1:1) = 17 mM.

M—Co PBA@OA	[M—Co PBA]: [OA]	TON_{CAT}/HER activity[a)]	Comments on the activity
Co—Co PBA@OA	1:4.6	68.6 ± 8.2	Inherent electrochemical properties and stability
Ni—Co PBA@OA	1:21	131.5 ± 10.5	Inherent electrochemical properties and stability
Cu—Co PBA@OA	1:2.3	2.5 ± 0.3[a)]	Low stability
Zn—Co PBA@OA	1:0.5	31.1 ± 13.1	Trivalent Co(III) acts as catalytic site

[a)]TON_{CAT} is given after 24 h.

incorporation into bilayer membranes, the intrinsic electrochemical properties of these metals remain uncompromised. In addition, they are stable because of lower dipole-dipole interaction compared to Zn—Co PBA and Cu—Co PBA[34] making them suitable to survive longer within the lipid water bilayer membrane. IR spectra of M—Co PBA@OA (Figure 5b) can be used to follow dipole-dipole interactions within the lattice, as the vibration of some water molecules coordinated to the M(II) in the structure was observed. The vibration of crystal water, $\nu(H_2O)$, was found at 3641 cm^{-1} for Co—Co PBA@OA and Ni—Co PBA@OA, whereas this signal was observed at 3647 and 3655 cm^{-1} for Zn—Co PBA@OA and Cu—Co PBA@OA respectively. This can be attributed to stronger Zn—OH_2 and Cu—OH_2 interactions (the presence of H_2O in these two M—Co PBA@OA structures in their organic solution is also prominent as evident from the ^1H NMR study, Figure S4, Supporting Information), indicating a higher dipole–dipole interaction with an order (Cu—Co PBA@OA > Zn—Co PBA@OA) and a high chance of spontaneous redox reactions at the membrane/water interface, leading to the loss of redox activity over time.[34] The strong interaction exhibited by Cu(II) in the PBA series makes it an effective adsorber, leading to chemical binding with H_2 gas.[2,35] This interaction can result in H_2 being trapped within the structure, making it difficult for H_2 to escape, thereby contributing to poor hydrogen evolution activity with a low TON of 2.5. Nevertheless, Zn(II) sites, which are relatively redox-inert, still facilitate H_2 production with TON = 31, supporting the idea that M^{II}–M^{III} PBAs exhibit bimetallic synergistic effects during photocatalytic HER as Co^{3+} ions can be reduced over M^{2+} during the reduction process. Once Co^{3+} accepts an electron, it reaches the $e_g^6\ t_{2g}^1$ electron configuration, corresponding to a low-spin Co(II) state (S = 1/2). This state has an unpaired electron, which readily participates in electron transfer processes, making it electrochemically active.[2,4,36] Moreover, the relatively larger particle size of Zn—Co PBA@OAs (Table 1) can also lead to a reduction in the number of surface-active sites, which can result in a decrease in TON.

This indicates that in addition to the inherent electrochemical properties of the divalent metals, the synergy of the trivalent Co(III), the particle size, and their stability across the water–membrane interphase, adsorption characteristics also play a significant role in determining the overall efficiency of the reaction systems.

To investigate the role of each photocatalytic component in photocatalytic HER, we selected our representative Ni—Co PBA@OA-based vesicle with lipid composition (DMPC: (14:0 PEG2000 PE) (100:1) and conducted several HER experiments with 1:1 (TEOA/$AscH_2$) under controlled conditions which are as follows: 1) RuC9 + Ni—Co PBA@OA in the dark, 2) only Ni—Co PBA@OA, 3) only RuC9, and 4) RuC9 + Ni—Co PBA@OA. The amount of H_2 produced (µmol) over time (h) against each condition is depicted in **Figure 6**a. Under the tested vesicle conditions (1–4), the following observations were made: in 1) RuC9 + Ni—Co PBA@OA in the dark and 2) only Ni—Co

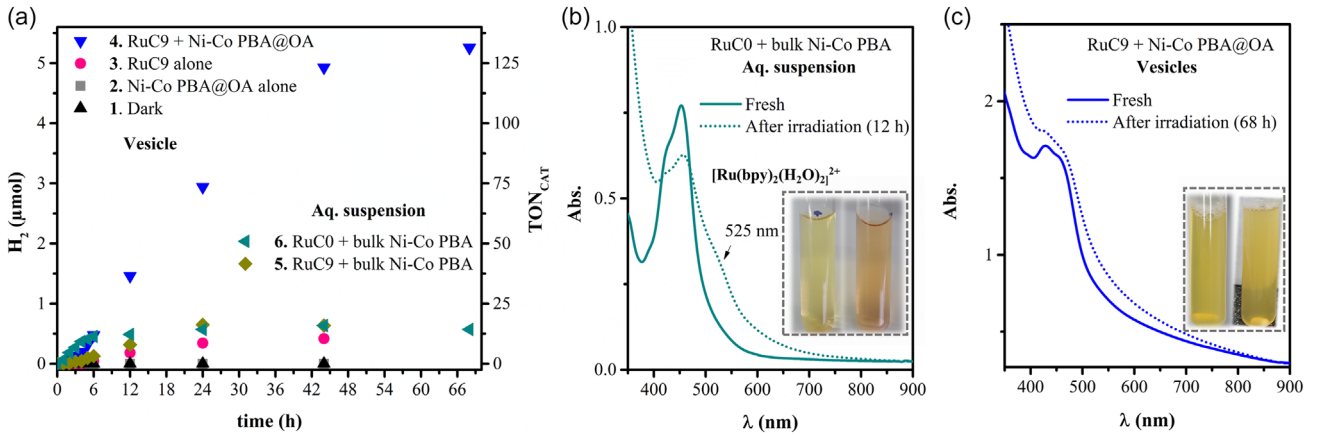

Figure 6. a) Time-dependent HER activity (μmol and TON_{CAT}) results of the DMPC vesicles (lipid composition = DMPC: (14:0 PEG2000 PE) (100:1)) monitored over 68 h, under various controlled experimental conditions: 1) RuC9 + Ni—Co PBA@OA in the dark, 2) Ni—Co PBA@OA alone, 3) RuC9 alone, 4) Ni—Co PBA@OA + RuC9 including their controlled aq. suspension system, and 5) RuC9 + bulk Ni—Co PBA, and 6) RuC0 + bulk Ni—Co PBA in the absence of any phospholipids. All values were acquired in Ar atmosphere. Reaction conditions: [RuC9/RuC0] = 55 μM, [Ni—Co PBA@OA or bulk Ni—Co PBA] = 10 μM, light source: 460 nm LED, [TEOA/AscH$_2$] (1:1) = 17 mM. b,c) UV–vis absorption spectra comparison of the aqueous suspension b) under condition (6) and vesicles c) under condition (4), both fresh and post-HER after 12 and 68 h of irradiation, respectively. Insets in each figure b,c) show photographs of the systems before (left) and after (right) irradiation.

PBA@OA, no H_2 was detected, whereas in 3) only RuC9, a small amount of H_2 (0.4 μmol over 44 h) was produced. These results indicate that light is essential for hydrogen production. The PS $Ru(bpy)_2(C9\text{-}bpy)^{2+}$ is capable of converting light into solar fuel through either side reactions or direct proton reduction,[37] albeit with a significantly low turnover number (TON_{PS}) of 1.9 (Figure S11b, Supporting Information). Ni—Co PBA@OA with RuC9 in the vesicle system 4) led to a nearly linear and steady increase in H_2 production over time. Over a 44 h period, 4.9 μmol of H_2 was generated, yielding a turnover number (TON_{PS}) of ≈22. This highlights the remarkable catalytic efficiency of Ni—Co PBA@OA, significantly boosting hydrogen production. To compare with the photocatalytic vesicle-controlled aq. suspension system, 5) RuC9 + bulk Ni—Co PBA and 6) RuC0 (the standard $[Ru(bpy)_3]^{2+}$) + bulk Ni—Co PBA were prepared, and their HER activity in the absence of any phospholipids was also monitored over time (Figure 6a). Under the standard PS condition (6), the Ni—Co PBA suspension produced 0.47 μmol of H_2 in 6 h, whereas the amphiphilic RuC9 (5) produced 0.64 μmol of H_2 in 24 h. Interestingly, in both cases, the H_2 production curve reached saturation quickly, whereas the photocatalytic vesicle exhibited sustained HER activity, continuing for nearly 2 days without a loss in kinetics. The TON_{CAT} after 68 h, as shown in Figure 6a and S11b, Supporting Information, clearly indicates that the photocatalytic vesicle of RuC9 + Ni—Co PBA@OA with TON_{CAT} 131 outperforms the aqueous suspensions by ≈9–10 times.

In the aqueous suspension with the standard PS (6), the HER ceased rapidly, and the yellow suspension shifted to a red color (see Figure 6b, inset). UV–vis spectra were recorded for both the fresh suspension and after 12 h of exposure during HER (Figure 6b). The spectra revealed a decrease in the absorption of the MLCT band, while a new shoulder band appeared at 525 nm, attributed to the formation of $[Ru(bpy)_2(H_2O)_2]^{2+}$.[8,38] This observation indicates an excitation deactivation process in the aqueous heterogeneous system, leading to the formation of an aqua-substituted product and reflecting inefficient electronic communication with the heterogeneous CAT. In contrast, the photocatalytic vesicle showed no such changes in color or absorption characteristics, even after 68 h of continuous light exposure (Figure 6c and inset). Additionally, the hydrodynamic diameters of the vesicles after HER were tested (Figure S12, Supporting Information), showing that the vesicles remained almost intact with slight changes in size distribution. Both of these results demonstrate high stability of the matrix and the local components like PS. This stability is likely a reason for the sustained activity over an extended period. Therefore, the enhanced and prolonged HER activity is attributed not only to the increased active sites of the CAT but also to the long-term stability of the PS, achieved through effective electronic communication across the bilayer.

The influence of CAT concentration (Ni—Co PBA@OA, 2–100 μM) on the photocatalytic HER of the vesicles was also investigated under similar reaction conditions: [PS] = 55 μM, lipid composition = DMPC: (14:0 PEG2000 PE) (100:1), [TEOA/AscH$_2$] (1:1) = 17 mM, with a 460 nm LED light source. The amount of H_2 produced (μmol), along with the TON_{CAT}, calculated over 24 h, was plotted against varying the CAT concentration as shown in **Figure 7**a. An increase in TON_{CAT} (77) was observed at lower CAT loading (2.5 μM), while at higher CAT loading (100 μM), the maximum amount of H_2 production reached 5.4 μmol, with a corresponding TON_{CAT} of 13.6. The results show that a low concentration of CATs allows for a high local concentration of coembedded catalytic subunits. This makes H_2 production more efficient and improves the activity of the CATs. However, the rapid decrease in TON_{cat} at higher CAT loadings can be attributed to the destabilization of the vesicle matrix. According to DLS measurements (Figure S13a, Supporting Information), the vesicle size at higher CAT concentrations (30 μM) was ≈188 nm as listed in Table S5, Supporting Information, significantly larger than vesicles with lower CAT loadings (2–10 μM). These larger vesicles

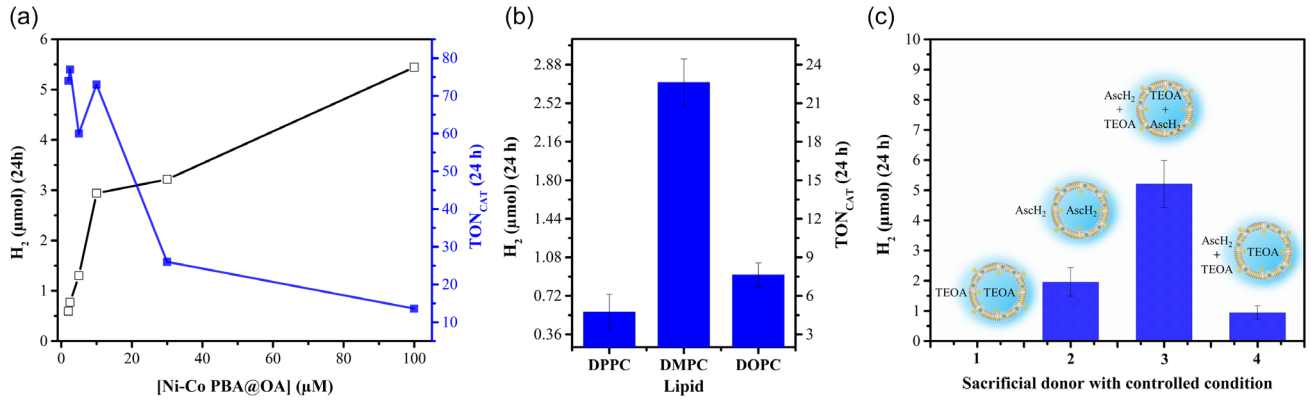

Figure 7. a) Effect of [Ni—Co PBA@OA] content on the HER activity (μmol of H_2 and TON_{CAT}) of the photocatalytic vesicle under following reaction conditions: [RuC9] = 55 μM, [Ni—Co PBA@OA] = *x* μM, light source: 460 nm LED, 24 h irradiation time, lipid = DMPC: (14:0 PEG2000 PE) (100:1), [TEOA/$AscH_2$] (1:1) = 17 mM, Ar atmosphere. b) Effect of the main phospholipid (DOPC, DMPC, and DPPC) on the TON_{CAT} and μmol of H_2 results under irradiation with 460 nm LED for 24 h for vesicles under following reaction conditions: [RuC9] = 55 μM, [Ni—Co PBA@OA] = 30 μM, lipid = (main lipid): (14:0 PEG2000 PE) (100:1), [TEOA/$AscH_2$] (1:1) = 17 mM, Ar atmosphere. c) Effect of sacrificial donors on HER activity (μmol of H_2) under 24 h of 460 nm LED irradiation, comparing as separated entities 1) TEOA alone and 2) $AscH_2$ alone and different local compositions (conditions (3) and (4); see the inset) of 1:1 TEOA/$AscH_2$. Experimental conditions: [RuC9] = 55 μM, [Ni—Co PBA@OA] = 100 μM, lipid composition = DMPC: (14:0 PEG2000 PE) (100:1), [sacrificial donor] = 17 mM, under an Ar atmosphere.

are more prone to structural disruption over prolonged light exposure. Additionally, at even higher CAT loadings (100 μM), the vesicles tend to form 2D film-like structures (Figure S13b,c, Supporting Information). TEM images of the sample at 100 μM show characteristic particle aggregation across the lipid films, further contributing to the reduced TON_{CAT} observed at elevated CAT concentrations.

As mentioned above, DMPC has zwitterionic head groups and a transition temperature around room temperature. HER activity of their photocatalytic vesicle was also examined with the main lipid being either the zwitterionic fluid phase DOPC and the zwitterionic gel phase DPPC, at fixed CATs (30 μM) and PS (55 μM) concentrations. Surprisingly both of them show a reduction in the H_2 evolution with $TON_{CAT} = 7.6$ (DOPC) and 4.7 (DPPC) in comparison to DMPC with $TON_{CAT} = 22.7$ after 24 h irradiation (Figure 7b). It has been reported that membrane fluidity or rigidity changes can positively influence photocatalytic activity, as seen in various studies.[39–41] For instance, with amphiphilic ruthenium-based PS, higher lipid bilayer mobility has been shown to promote light-driven reduction reactions, facilitating intermolecular electron transfer dynamics within the soft matter matrix.[39,40] Conversely, a more rigid lipid bilayer, as in oleic acid-capped quantum dots, offers protection to the PS nanomaterials, resulting in increased hydrogen evolution.[41] In our study, however, no such trend was observed. The fluid, mobile aggregation state of DOPC membranes performed just as poorly as the rigid, gel-phase DPPC membranes. These unexpected results mirror recent observations within our group when working with similar amphiphilic PS and a $Mo_3S_{13}^{2-}$-based CATs.[20] This behavior in our case can be attributed to the inherent limitations of the lipids themselves. DOPC, due to its lower phase transition temperature and unsaturated tails, creates a more fluid and permeable membrane and smaller vesicle than DMPC (Table S6 and Figure S14, Supporting Information), which may impede the proper incorporation and stabilization of PBA-based nanomaterial at the membrane.[42,43] On the other hand, in our study, DPPC tends to form larger and less stable vesicles than DMPC, and extrusion—where lipid mixtures are forced through membranes for uniform size—leads to loss of the local components and most importantly collapse over prolonged exposure to light (Table S6 and Figure S14).[44] Thus, only the lipid membrane operating at its transition temperature, DMPC, offers a favorable environment. The fluidity of DMPC allows for better control over vesicle size, promotes uniform incorporation of M—Co PBA, and facilitates intermolecular electron transfer dynamics, all of which collectively enhance hydrogen production significantly.

To investigate the role of sacrificial donors in HER, the photocatalytic vesicle system was initially tested with two separate donors: 1) TEOA and 2) $AscH_2$. Under 24 h of irradiation, the yield of H_2 was ≈2 μmol in the presence of $AscH_2$, while no H_2 production was detected with TEOA alone (Figure 7c). This can be attributed to the larger molecular size of TEOA and its low permeability across the membrane, as supported by previous studies.[45–47] However, when a 1:1 combination of TEOA and $AscH_2$ (3) was used, the hydrogen yields increased 2.7 times. To further validate these findings, a vesicle with varying compositions of TEOA and $AscH_2$ across the inner and outer compartments, maintaining the same 1:1 ratio, was prepared. By adding TEOA during the rehydration process and subsequently diluting with $AscH_2$, a highly localized concentration of TEOA was established within the inner compartment, while a relatively higher concentration of $AscH_2$ was maintained in the outer compartment (4). The HER results of the prepared vesicle showed a ≈5-fold reduction in HER activity, indicating that the 1:1 combination likely forms a conjugate acid–base pair [$AscH^-$][$TEOAH^+$] in an aq. solution, which affects the electron-donating properties of $AscH_2$. $AscH_2$'s electron-donating ability is optimal in its deprotonated form (ascorbate), as demonstrated in prior reports.[20,45] Control studies using the

sodium salt of ascorbate ($AscH^-$) showed that the HER activity of the photocatalytic vesicle can be increased by 1.5 times (Figure S15, Supporting Information), further supporting this hypothesis.

The HER activity of the representative Ni—Co PBA@OA-based photocatalytic vesicle, containing 55 μM of RuC9, a lipid composition of DMPC: (14:0 PEG2000 PE) (100:1), and 17 mM of 1:1 TEOA/$AscH_2$, was monitored over 68 h of irradiation using three LED light sources with excitation wavelengths of 405–415, 460, and 530 nm (Figure S16, Supporting Information). The turnover numbers (TON_{CAT}) and the amount of H_2 produced (μmol) after 68 h are presented in **Figure 8**a. The TON_{CAT} values were 201 at 405–415 nm, 131 at 460 nm, and 31 at 530 nm. These results show an almost fourfold decrease in TON_{CAT} at the absorption edge (530 nm) of RuC9 and a 1.5-fold increase in TON_{CAT} at 405–415 nm, where the MLCT state of RuC9 is fully populated. This demonstrates again that RuC9 within the photocatalytic vesicle is solely responsible for light absorption and that the populated MLCT excited states play a crucial role throughout the photocatalytic HER process.

The HER activity of the photocatalytic vesicle exhibited significant durability, with a nearly linear increase in H_2 production observed over the initial 44 h. However, beyond this point, the rate of H_2 generation decreased, and by 68 h of irradiation, no significant H_2 production was detected. UV–vis studies of the photocatalytic vesicles conducted after 68 h qualitatively confirmed the presence of RuC9 (Figure 6c), indicating that at least one additional component of the photocatalytic system experienced decomposition or consumption, which restricted its sustained activity. To gain insight into the limitations of photocatalysis, we introduced either an additional equivalent of 1) fresh CAT (Ni—Co PBA@OA), 2) donor (1:1 TEOA/$AscH_2$), or 3) fresh PS (RuC9) to the reaction mixture following an initial photocatalytic run with our representative photocatalytic vesicle. To achieve the replenishment of active components, we implemented a protocol recently established by Klein et al.[48] A thin film of either RuC9 or Ni—Co PBA@OA was deposited in a glass pressure-resistant tube. The irradiated vesicle mixture was subsequently added to the tube, and the solution was heated for 1 h at 50 °C, accompanied by gentle ultrasonication. Our objective was to maximize the incorporation of PS or CAT molecules from the thin film into the vesicles. The initiation of the second cycle followed. Conversely, donor replenishment occurs via direct injection of fresh donor molecules, disregarding minimal dilution, and is succeeded by the commencement of the second cycle. Upon resuming light irradiation, the addition of extra RuC9 or the sacrificial donor resulted in an extended photocatalytic activity, yielding supplemental TON_{CAT} values of 44 and 18, respectively. In contrast, the addition of extra Ni—Co PBA@OA did not produce any significant amount of H_2 (Figure 8b). These experiments demonstrated that the loss of catalytic activity results from the partial decomposition of the PS and the consumption of the donors, indicating that the CAT was not the limiting factor in H_2 production under these conditions.

2.4. Photoinduced Charge Transfer Dynamics

To elucidate the photoinduced charge transfer dynamics of the photocatalytic components within the lipid bilayer matrix, vesicles composed of DMPC: PEG (100:1) containing RuC9 were investigated using steady-state and time-resolved emission and absorption spectroscopy under various conditions: In the presence of no quencher, Ni—Co PBA@OA, $AscH_2$, TEOA/$AscH_2$ (1:1), or Ni—Co PBA@OA + TEOA/$AscH_2$ (1:1). In principle, it is possible that upon PS excitation, the initial electron transfer takes place either from the sacrificial electron donor to the excited

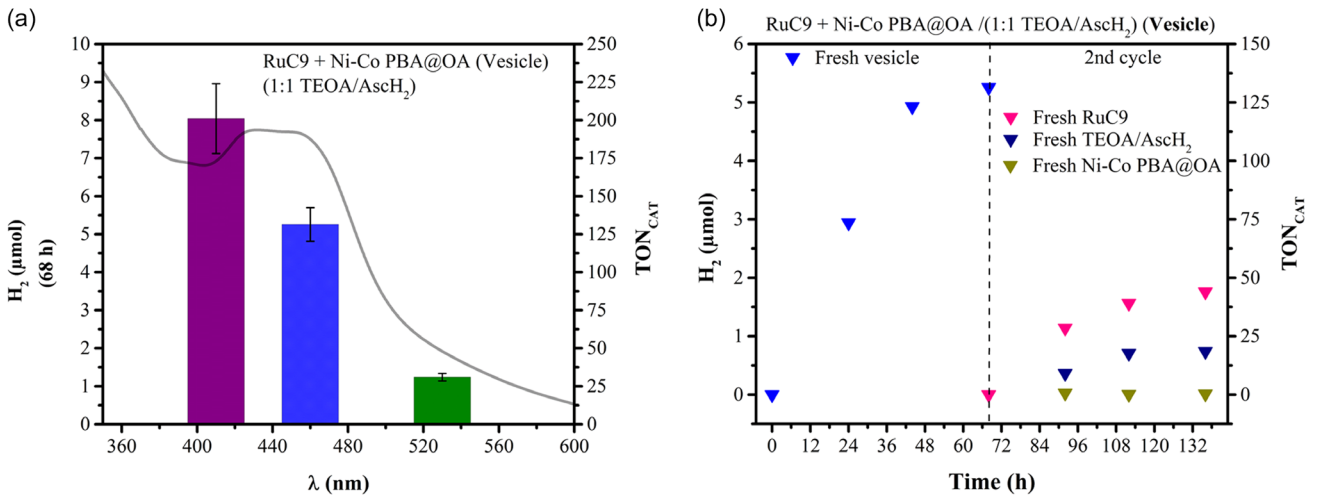

Figure 8. a) Hydrogen evolution (in μmol) and TON_{CAT} results for Ni—Co PBA@OA-based photocatalytic vesicles after 68 h of irradiation using three different LED light sources with excitation wavelengths of 405–415 nm (violet), 460 nm (blue), and 530 nm (green). Reaction conditions: [RuC9] = 55 μM, [Ni—Co PBA@OA] = 10 μM, lipid composition = DMPC: (14:0 PEG2000 PE) (100:1), and [TEOA/$AscH_2$] (1:1) = 17 mM. b) Repeated HER using photocatalytic vesicles with the same components as described above under 460 nm LED light irradiation. After the first cycle, the samples were replenished with one of the following components: 1) 10 μM of Ni—Co PBA@OA (dark yellow curve), 2) 17 mM of [TEOA/$AscH_2$] (1:1) (navy curve), or 3) 55 μM of RuC9 (pink curve). Photocatalysis was resumed after replenishment.

PS (reductive quenching) or from the excited PS to the CAT (oxidative quenching).

Steady-state emission spectra and kinetics of the RuC9 in DMPC: (14:0 PEG2000 PE) (100:1) vesicles were recorded in the presence of various electron donors and acceptors as depicted in **Figure 9**a,b, respectively. The emission of RuC9 at 634 nm, with a lifetime (τ) of 499 ns, was found to be slightly quenched in the presence of the donor molecule ($AscH_2$), reducing the lifetime to 465 ns. A more pronounced quenching effect was observed with the aqueous mixture of TEOA/$AscH_2$, further shortening the lifetime to 380 ns. The observed decrease in both emission intensity and lifetime suggests the involvement of dynamic quenching mechanisms in the presence of these donor molecules. Without any donor molecules, the presence of Ni—Co PBA@OA leads to a hypsochromic shift (≈9 nm) in the emission band of RuC9 to 425 nm, along with an increase in luminescence intensity and extended lifetime (567 ns). This result aligns with the observations from UV–vis absorption in Figure 3d, where we noted that OA-capped Ni—Co PBA enhances membrane fluidity and influences the MLCT transition. This increase in fluidity and the presence of the OA-capped nanoparticles seem to increase the quantum yield and lifetime for the luminescent excited state. Interestingly, the increase in fluidity in the RuC9 + Ni–Co PBA@OA vesicles significantly accelerates the reductive

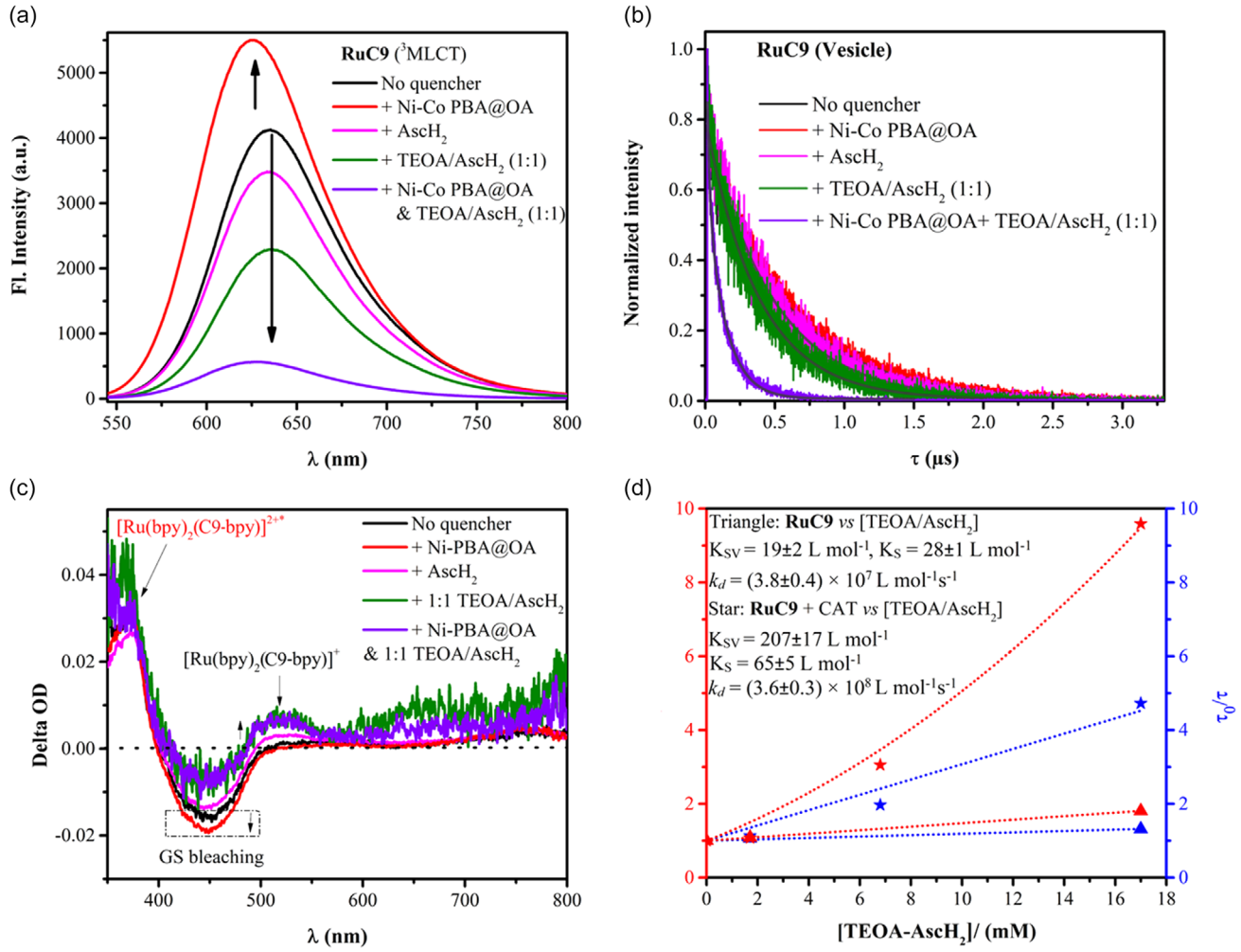

Figure 9. a) PL spectra of DMPC: (14:0 PEG2000 PE) (100:1) vesicles containing 55 μM RuC9 under different conditions: 1) no quencher, 2) [Ni—Co PBA@OA] (5 μM), 3) $AscH_2$ (17 μM), 4) [TEOA/$AscH_2$] (17 mM), and 5) [Ni—Co PBA@OA] (5 μM) with all other parameter's constant (Ar atmosphere, $\lambda_{exc} = 450$ nm). b) Lifetime measurements of 55 μM RuC9 in DMPC: (14:0 PEG2000 PE) (100:1) vesicles under the same conditions as described in (a). The PL decay curves were fitted to a single-exponential and a biexponential decay functions in origin software(see Supporting Information for details and fitting parameters). c) Nanosecond transient absorption spectra (ns-TA) of vesicles (DMPC: (14:0 PEG2000 PE) (100:1)) containing 55 μM RuC9 under the same experimental conditions as in (a). d) Stern–Volmer plot for vesicles (DMPC: (14:0 PEG2000 PE) (100:1)) vesicles containing 1) 55 μM RuC9 alone and 2) 55 μM RuC9 with 5 μM Ni—Co PBA@OA as a function of [TEOA/$AscH_2$] concentration. The plot of $\frac{\tau_0}{\tau}$ vs [Q] for 1 and 2 is fitted using a linear curve following the equation ($\frac{\tau_0}{\tau} = 1 + K_{SV}[Q]$); k_d is calculated from the formula $K_{SV} = k_d\tau_0$. The plot of $\frac{I_0}{I}$ vs $[Q]$ for 1 and 2 is fitted using a linear curve ($\frac{I_0}{I} = 1 + (K_{SV} + K_s)[Q]$) and a polynomial curve ($\frac{I_0}{I} = 1 + (K_{SV} + K_s)[Q] + (K_{SV} \times K_S)[Q]^2$), respectively. K_S is calculated by solving the respective equation with the obtained K_{SV} values. Experimental conditions: $\lambda_{exc} = 450$ nm, Ar atmosphere.

quenching by the donor mixture of aq. TEOA/$AscH_2$, resulting in a more efficient electron transfer process, as evidenced by the markedly reduced lifetime of 120 ns.

Nanosecond-transient absorption spectroscopy confirmed the assignment of reductive emission quenching via electron transfer from the electron donors to the PS. The spectra shown in Figure 9c were recorded in the first 100 ns after the laser pulse ($\lambda = 450$ nm) and show the ground state (GS) bleach at 450 nm and excited state absorption at 370 nm in case of no quencher or CAT. In the presence of an electron donor, however, there is an additional positive feature at 510 nm, which is indicative of the reduced PS photoproduct, confirming electron transfer to the PS.[2] The intensity of the photoproduct feature ($[Ru(bpy)_2(C9\text{-}bpy)]^+$) at 510 nm is highest in the presence of the donor mixture TEOA + $AscH_2$, which is in line with the steady-state quenching data. However, in the presence of Ni—Co PBA@OA, even though the quenching efficiency dramatically increases by the donor mixture TEOA + $AscH_2$ (Figure 9a,b), the population of the photoproduct remains almost the same (Figure 9c). This observation not only supports the validity of the initial reduction quenching mechanism but also illustrates the second step of the electron transfer process occurring between the light-driven and dark reactions.

The results thus far indicate that the PS in the vesicle is quenched by the sacrificial donor molecule through a reductive quenching mechanism, with no evidence of oxidative quenching in the presence of Ni—Co PBA@OA CAT. However, under actual HER conditions—where both components (donor and CAT) are present at their fixed concentrations—an indirect cooperative interaction likely occurs, leading to a dramatic increase in quenching of the excited PS by the sacrificial donor molecule.

To get additional insights on the electron transfer dynamics between PS and electron donor in the vesicle, a Stern–Volmer assay was conducted under two conditions: 1) RuC9 and 2) RuC9 with Ni—Co PBA@OA (see Figure S17a,b, Supporting Information, for the typical dataset for the photoluminescence (PL) decay curve, and the fitting parameters for the decay curves are listed in Table S7, Supporting Information). For this assay, the steady state emission and time resolved emission quenching, $\frac{I_0}{I}$ and $\frac{\tau_0}{\tau}$ respectively, are plotted at various donor concentrations $[Q] = [1{:}1\ TEOA/AscH_2]$ (Figure 9d) and fitted with the Stern–Volmer models:[49–51]

$$\frac{\tau_0}{\tau} = 1 + K_{SV}[Q] \quad (1)$$

$$K_{SV} = k_d \tau_0 \quad (2)$$

$$\frac{I_0}{I} = 1 + (K_{SV} + K_s)[Q] \quad (3)$$

$$\frac{I_0}{I} = 1 + (K_{SV} + K_s)[Q] + (K_{SV} \times K_S)[Q]^2 \quad (4)$$

Here, I_0 and I are emission intensities in the absence and presence of the quencher, respectively, while τ_0 and τ correspond to the excited-state lifetimes in the absence and presence of the quencher, respectively. When plotting the ratio $\frac{\tau_0}{\tau}$ against $[Q]$, the resulting graphs display a linear relationship in both cases. However, the relative change observed in these ratios is not proportional to the corresponding change in relative fluorescence intensity $\left(\frac{I_0}{I}\right)$.This discrepancy is particularly pronounced in case 2, where a notable upward or positive deviation is evident. This observation suggests that both static and dynamic quenching mechanisms contribute to the observed decrease in emission intensity and both of these quenching increases significantly when the vesicle contains both PS and CAT. Applying the Stern–Volmer equation (Equation (1)) as a linear regression for $\frac{\tau_0}{\tau}$ vs $[Q]$ curve yields the Stern–Volmer constant (K_{SV}) as a slope, and the subsequent dynamic quenching constant k_d can be calculated from Equation (2), while the association constant (K_S) for conditions (1) and (2) is estimated from Equation (3) and (4) by fitting $\frac{I_0}{I}$ against $[Q]$ plots using a linear and a polynomial curve, respectively (see Table S8, Supporting Information).

The dynamic quenching constant (k_d) estimated for the vesicle containing only PS is $(3.8 \pm 0.4) \times 10^7\ L\,mol^{-1}\,s^{-1}$, with a corresponding K_{SV} of $19 \pm 2\ L\,mol^{-1}$ and K_S of $28 \pm 1\ L\,mol^{-1}$. In contrast, for the vesicle containing both PS and CAT, the dynamic quenching constant increases nearly tenfold to $(3.6 \pm 0.3) \times 10^8\ L\,mol^{-1}\,s^{-1}$, with K_{SV} and K_S rising to 207 ± 17 and $65 \pm 5\ L\,mol^{-1}$, respectively. This significant enhancement in dynamic quenching efficiency can be attributed to the increased fluidity of the membrane.[52] The lateral mobility of both the quencher and PS is greater in more fluidic membranes, facilitating more frequent encounters. Consequently, the introduction of OA-modified CAT enhances mobility, allowing the quencher to interact with the fluorophore more often, leading to more efficient dynamic quenching.

In summary, we conclude on the following photocatalytic reaction process, which is also depicted in **Figure 10**. Upon light irradiation, RuC9 is excited, generating the excited state $RuC9^*$ ($[Ru(bpy)_2(C9\text{-}bpy)]^{2+*}$). Monoascorbate ($AscH^-$), generated from 1:1 TEOA/$AscH_2$ as discussed earlier, acts as an electron sacrificial reagent, reducing $[Ru(bpy)_2(C9\text{-}bpy)]^{2+*}$ to $[Ru(bpy)_2(C9\text{-}bpy)]^+$. This reduction occurs through both static and dynamic pathways. DMPC with 14:0 PEG2000 PE at 100:1 serves as an optimized lipid, providing a suitable membrane for incorporating the OA-capped Ni—Co PBA as a representative CAT among the four M—Co PBA@OAs (M = Co, Ni, Cu, and Zn). The presence of OA across the membrane significantly enhances the dynamic quenching process, cooperating in the generation of a higher amount of active reduced species $[Ru(bpy)_2(C9\text{-}bpy)]^+$. This species subsequently transfers electrons to the ultrafine OA-capped Ni—Co PBA Gnanoparticles (≈1 nm) via dark reaction (as evident from the ns-transient absorption spectra, Figure 9c) for HER, while returning to RuC9 ($[Ru(bpy)_2(C9\text{-}bpy)]^{2+}$). In contrast, under aqueous suspension conditions with bulk Ni—Co PBA (≈240 nm) and aq. RuC0, such dark reactions are sluggish due to a limited number of active sites and pore restrictions, which can lead to substantial degradation of the PS through the loss of bipyridine molecules as evidenced in UV–vis absorption spectra and fast deactivation (within 6 h) in HER. These findings clarify the reasons for the observed ninefold to tenfold increase in efficiency and the extended duration of HER (over 2 days) without a loss in kinetics within the photocatalytic vesicle system.

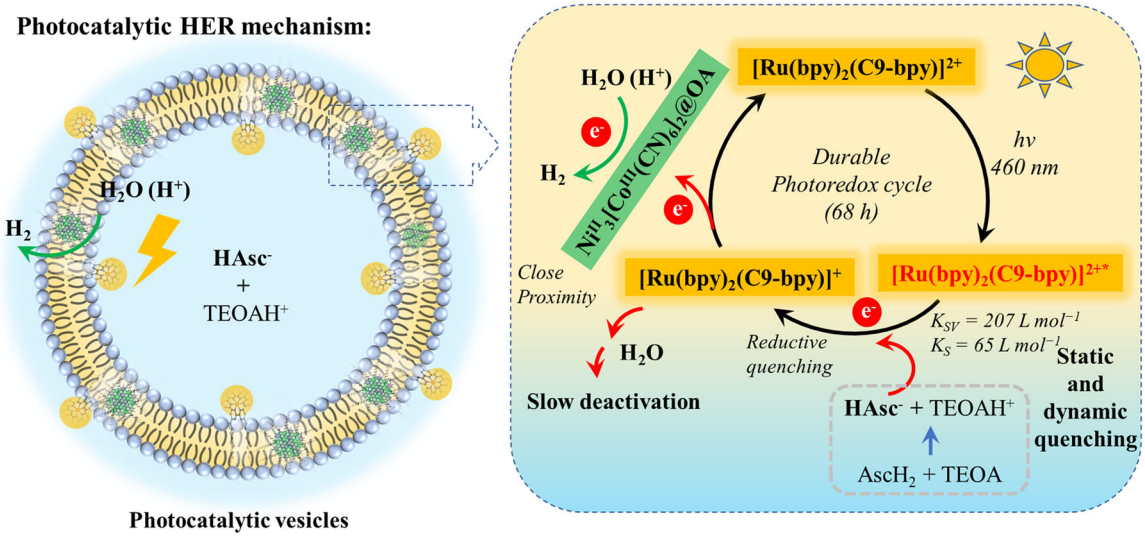

Figure 10. Schematic illustration of the photocatalytic HER with the representative vesicle system. The vesicle consists of a DMPC: (14:0 PEG2000 PE) (100:1) bilayer encapsulating 55 μM RuC9 as the PS, 5 μM Ni—Co PBA@OA as the co-CAT, and 17 Mm TEOA/$AscH_2$ (1:1) as the electron donor system, all under an inert Ar atmosphere.

3. Conclusion

In conclusion, this study presents a novel approach to embedding OA-capped M—Co PBA nanoparticles into phospholipid bilayers for use in light-driven hydrogen evolution. By integrating these hydrophobic nanoparticles within DMPC and 14:0 PEG2000 PE vesicles and combining them with an amphiphilic PS, we successfully demonstrated enhanced HER activity, especially with Ni—Co PBA@OA, which exhibited a significantly higher TON (≈131) and superior stability. The close proximity of the CAT and PS, driven by hydrophobic interactions, resulted in a marked improvement in catalytic efficiency, with a ninefold increase in hydrogen production compared to conventional systems. The sustained HER activity, lasting over 68 h, is attributed to multiple factors, including efficient electron transfer, the enhanced stability of the PS, and the robust scaffold design. This work offers new insights into the design of artificial photosynthetic systems and highlights the potential for optimizing CAT-PS interactions for improved photocatalytic performance.

4. Experimental Section

Preparation of OA-Capped Ultrafine M—Co PBA Nanoparticles (M—Co PBA@OA): In step 1 (Figure 2a), a precipitation route as reported earlier[53,54] was followed to synthesize the bulk M—Co PBA with the general formula $M^{II}_3[Co^{if}(CN)_6]_2{\cdot}nH_2O$ (see SI for details). Inspired by some earlier reports[29,55,56] of postsynthetic modification of the PBA, we chose OA ($CH_3(CH_2)_7CH{=}CH(CH_2)_8NH_2$) as a stabilizing agent and adopted a slightly modified route (step 2, Figure 2a). Briefly, in a 100 mL round bottle, prepared bulk M—Co PBA powder (100 mg) was dispersed in 4–25 mL of polar and protic solvent (MeOH or H_2O) by ultrasonic treatment for 15 min. After that, an *n*-hexane or $CHCl_3$ solution (34–40 mL) of OA (80–160 μL) was added to the M—Co PBA suspension. This immediately created a biphasic mixture (MeOH-*n*-hexane or H_2O—$CHCl_3$) where the M—Co PBA remained in the polar solvent, while the OA preferred the nonpolar solvent. As stirring continued, the M—Co PBA gradually migrated to the nonpolar solvent. After stirring the biphasic suspension for 1–3 days at ambient temperature and air (≈25 °C) (see Supporting Information, for details on each experimental parameter for the surface functionalization experiment of M—Co PBAs), the $CHCl_3$ or *n*-hexane solution of M—Co PBA@OA was separated from the aqueous or methanolic phase and dried under reduced pressure using a rotary evaporator for 1 h. The dried solid samples of M—Co PBA@OA were subjected to solid-state characterization methods, such as ATR-IR and PXRD. For further use, the samples were dissolved in 11 mL of $Chicly_3$ and centrifuged at 15 000 rpm for 15 min to remove large particles (step 3, Figure 2a). The resulting transparent solution of M—Co PBA@OA was used as a stock solution for integrating into vesicles. Notably, this stock solution was also used for structural characterization via DLS and ^{1}H NMR. The OA content in the stock solution of M—Co PBA@OA was quantified using ^{1}H NMR with nitrobenzene as an internal standard to calculate the concentration of CATs in the stock solution (see Supporting Information, for calculation details). Additionally, HR-TEM techniques were employed to analyze the particle nature of the $chicle_3$ solution of Ni—Co PBA.

Preparation of 10% of 2-Aminoanthracene-Tagged Ni—Co PBA@OA: Before the postsynthetic modification Ni—Co PBA by OA, Ni—Co PBA powder (100 mg) was first dispersed in EtOH and treated with 2-aminoanthracene (10 mg) and kept under stirring overnight (≈12 h) at room temperature.[32] The final suspension was then centrifuged at 15 000 rpm and washed with EtOH several times. Finally, greenish powder (2-aminoanthracene tagged Ni—Co PBA) obtained after drying under vacuum was used for further modification with the same protocol mentioned above. The prepared compound was characterized in the solid-state using ATR-IR and PXRD analyses. Additionally, the stock solution in $chicly_3$ was utilized for vesicle preparation and thereafter for confocal fluorescence microscopy studies.

Preparation of Stock Solutions of the Components for Vesicle Preparations: Stock solutions of 33 mM of lipid (DMPC) and 0.66 mM of 14:0 PEG2000 PE were prepared in $CHCl_3$, and they were stored at 4 °C. Besides DMPC, relatively longer hydrocarbon chain-based zwitterionic lipids such as DPPC and DOPC were also tested, and their stock solution was prepared. The synthesis of the PS $Ur^i(buy)_2(boy\text{-}C_9)_2$ was performed as previously described by our group.[23] A stock solution of 0.66 mM of PS($[Ru(buy)_2(C9\text{-}bpy)]$ $(PF_6)_2$) in CH_3CN and 0.1 M of aqueous TEOA and/or $AscH_2$ as electron donor were prepared, separately. The CAT stock

solution (M—Co PBA@OA) was prepared in $chicle_3$ at concentrations ranging from 2.4 to 14.6 mM and used as such.

Vesicle Preparation: All the steps involved in vesicle preparation were outlined in Scheme S1, Supporting Information, and have been previously utilized by our group.[20] Briefly, in a 25 mL of round bottle, 1 mL of 0.66 mM 14: 0 PEG2000 and 2 mL of 33 mM DMPC lipid were mixed and stirred for 15 min. In another round bottle, 1 mL of 0.66 mM of $Ru[(bpy)_2(C9\text{-}bpy)](PF_6)_2$ in CH_3CN was evaporated under reduced pressure and mixed with 0.008–0.05 µL of M—Co PBA@OA stock solution (2.4–14.6 mM) and made the volume to 1 mL by the addition $CHCl_3$. The resultant mixture after stirring for 15 min was added to the lipid solution slowly and kept for 30 min for stirring to make a homogenous mixture of all the components. Afterward, the solvent was evaporated using a rotary evaporator, followed by 20 min of high vacuum on a Schlenk line to form the film. The resulting film was then rehydrated with 4 mL of an aqueous solution containing 0.1 M TEOA and 0.1 M $AscH_2$, applied only for photocatalytic HER and spectroscopic (mechanistic) studies. The resultant photocatalytic lipid suspension was frozen using liquid N_2 and thawed with a water bath at 10 °C above the transition temperature (T_m) of the lipid. This step was repeated seven times until the solution was homogeneous. To obtain a more uniform size distribution, transitioning from MLVs to unilamellar vesicles (ULV), extrusion was performed 11 times using a mini extruder equipped with a heating block from Avanti Polar Lipids. The extrusion process utilized nucleopore polycarbonate track-etch membranes with a pore size of 1 µm, along with filter supports featuring a pore size of 10 mm. After preparation, every sample was stored at 4 °C for a maximum of 1 week. For all studies, the final vesicle samples were diluted by deionized water three times. For structural characterizations, steady-state UV–vis absorption, TEM, and confocal fluorescence microscopic imaging was performed on vesicles prepared in the following way: 14:0 PEG2000 and DMPC lipid were used to make the film, which was then rehydrated with deionized water instead of the sacrificial donor solution and followed the same steps to achieve the vesicle. In addition, for confocal fluorescence microscopic studies, instead of Ni—Co OBA@OA, a 10% 2-aminoanthracene-tagged Ni—Co PBA@OA has been used to integrate into the vesicle.

Photocatalytic HER: For HER experiments, the prepared vesicle solutions (4 mL) were purged carefully with Ar gas for 30 min and diluted three times with deaerated water under an Argon atmosphere within a glove box (O_2 content < 0.5 ppm). Four milliliters (4 mL) of it was then transferred to the 8 mL of WICOM WIC 41 600/333 clear glass screw neck GC vial (ND13). The vial was then sealed, transferred into a 3D-printed photoreactor using two ring holders, and irradiated by LZ1-00DB00 Dental Blue as an LED light source ($\lambda = 460$ nm, 800–1250 mW) with a current of 0.7 A and voltage of 4 V while stirring for 68 h. The experiment was performed at room temperature via a ventilation system in the back of the reactor. At different time intervals, the evolved H_2 was analyzed using headspace GC for each reaction vessel. The analysis was performed on a Shimadzu GC-2030 system equipped with a barrier ionization discharge (BID-2030) detector and helium as the carrier gas. A 100 µL sample of the headspace was manually injected for each measurement. TONs were calculated as the ratio of mols of H_2 produced to mols of the $M_3[Co(CN)_6]_2$ CATs. The final composition of the vesicles was DMPC (5.5 mM), 14:0 PEG2000 (55 µM), RuC9 (55 µM), and M—Co PBA@OA (10 µM). Several control experiments were conducted within the vesicles, along with comparative studies using aqueous suspensions of their active components. For the aqueous suspension, an equivalent amount of PS, either $[Ru(bpy)_3]^{2+}$ or $[Ru(bpy)_2(C9\text{-}bpy)]^{2+}$, along with the bulk CAT (Ni—Co PBA), was prepared in 4 mL of aqueous sacrificial donor solution. We irradiated these solutions under the same experimental conditions as the vesicle-based experiments to ensure comparability. In addition to the control studies, various experimental conditions were systematically examined to assess their impact on the system. These conditions included the following: 1) Lipid variations: different types of lipids were used to form the vesicles, such as DPPC and DOPC, allowing the investigation of how other lipid affects vesicle formation and functionality. 2) CAT concentration: the concentration of the best CAT among the M—Co PBA@OA was varied to determine its influence on the overall system performance, including its interaction with the PS and vesicle membrane. 3) Sacrificial donor variations: different sacrificial donors were tested, along with separate additions of TEOA, $AscH_2$, and sodium ascorbate (NaHAsc) to evaluate how these donors influence the photocatalytic process and hydrogen evolution. 4) LED light sources with different excitation wavelengths: 405–415 nm (900 mW, with a current of 0.4 A and a voltage of 14 V), 460 nm (800–1250 mW, with a current of 0.7 A and a voltage of 4 V), and 530 nm (281 mW, with a current of 0.5 A and a voltage of 3.4 V).

Supporting Information

Supporting Information is available from the Wiley Online Library or from the author.

Acknowledgements

A.P. gratefully acknowledges the Vector Stiftung (project number P2019-0110) and the Carl-Zeiss Stiftung for financial support. A.P. and U.K. gratefully acknowledge the Deutsche Forschungsgemeinschaft (DFG) funding through project TRR234 "CataLight" project number 364549901, projects B8 and Z2. The confocal images were taken at Ulm University's Core Facility for Confocal and Multiphoton Microscopy. The DFG funds this facility through project number 91BGG INST 381/39-1. The authors thank Dr. Sviatlana Kalinina and Dr. Christian Bökel for their support during confocal microscopy. The authors also thank Renate Kunz and Paul Walther from the Central Facility for Electron Microscopy, Ulm University, for help with transmission electron microscopy measurements.

Conflict of Interest

The authors declare no conflict of interest.

Author Contributions

Subrata Mandal: conceptualization (equal); data curation (lead); formal analysis (lead); investigation (lead); methodology (lead); supervision (supporting); visualization (lead); writing—original draft (lead); writing—review & editing (equal). **Akash Deshpande**: data curation: (supporting); investigation (supporting). **Robert Leiter**: data curation (supporting); formal analysis (supporting); methodology (supporting); writing—original draft (supporting). **Johannes Biskupek**: data curation (supporting); formal analysis (supporting); investigation (supporting); methodology (supporting); project administration (supporting); supervision (supporting); writing—original draft (supporting). **Ute Kaiser**: funding acquisition (equal); methodology (supporting); project administration (equal); resources (equal); supervision (equal). **Andrea Pannwitz**: conceptualization (equal); investigation (equal); project administration (lead); resources (lead); supervision (lead); writing—review & editing (lead).

Data Availability Statement

The data that support the findings of this study are available in the supplementary material of this article.

Keywords

hydrogen, liposomes, prussian blue analogs, photocatalysis

Received: October 31, 2024
Revised: February 13, 2025
Published online: March 17, 2025

[1] S. E. Hosseini, M. A. Wahid, *Renewable Sustainable Energy Rev.* **2016**, *57*, 850.
[2] X. Meng, J. Yang, C. Zhang, Y. Fu, K. Li, M. Sun, X. Wang, C. Dong, B. Ma, Y. Ding, *ACS Catal.* **2022**, *12*, 89.
[3] A. A. Ahmad, T. G. Ulusoy Ghobadi, M. Buyuktemiz, E. Ozbay, Y. Dede, F. Karadas, *Inorg. Chem.* **2022**, *61*, 3931.
[4] S. Goberna-Ferrón, W. Y. Hernández, B. Rodríguez-García, J. R. Galán-Mascarós, *ACS Catal.* **2014**, *4*, 1637.
[5] M. Zhang, Y. Chen, J.-N. Chang, C. Jiang, W.-X. Ji, L.-Y. Li, M. Lu, L.-Z. Dong, S.-L. Li, Y.-P. Cai, Y.-Q. Lan, *JACS Au* **2021**, *1*, 212.
[6] Y. Yamada, K. Oyama, T. Suenobu, S. Fukuzumi, *Chem. Commun.* **2017**, *53*, 3418.
[7] A. Soupart, F. Alary, J.-L. Heully, P. I. P. Elliott, I. M. Dixon, *Inorg. Chem.* **2018**, *57*, 3192.
[8] B. Durham, J. V. Caspar, J. K. Nagle, T. J. Meyer, *J. Am. Chem. Soc.* **1982**, *104*, 4803.
[9] A. Solé-Daura, Y. Benseghir, M.-H. Ha-Thi, M. Fontecave, P. Mialane, A. Dolbecq, C. Mellot-Draznieks, *ACS Catal.* **2022**, *12*, 9244.
[10] E. Mamontova, F. Salles, Y. Guari, J. Larionova, J. Long, *Inorg. Chem. Front.* **2022**, *9*, 3943.
[11] A. Pannwitz, D. M. Klein, S. Rodríguez-Jiménez, C. Casadevall, H. Song, E. Reisner, L. Hammarström, S. Bonnet, *Chem. Soc. Rev.* **2021**, *50*, 4833.
[12] N. Sinambela, J. Bösking, A. Abbas, A. Pannwitz, *ChemBioChem* **2021**, *22*, 3140.
[13] S. Rodríguez-Jiménez, H. Song, E. Lam, D. Wright, A. Pannwitz, S. A. Bonke, J. J. Baumberg, S. Bonnet, L. Hammarström, E. Reisner, *J. Am. Chem. Soc.* **2022**, *144*, 9399.
[14] N. Ikuta, S. Takizawa, S. Murata, *Photochem. Photobiol. Sci.* **2014**, *13*, 691.
[15] B. Limburg, J. Wermink, S. S. van Nielen, R. Kortlever, M. T. M. Koper, E. Bouwman, S. Bonnet, *ACS Catal.* **2016**, *6*, 5968.
[16] H. Song, A. Amati, A. Pannwitz, S. Bonnet, L. Hammarström, *J. Am. Chem. Soc.* **2022**, *144*, 19353.
[17] S. Takizawa, T. Okuyama, S. Yamazaki, K. Sato, H. Masai, T. Iwai, S. Murata, J. Terao, *J. Am. Chem. Soc.* **2023**, *145*, 15049.
[18] S. R. González, P. J. Aymonino, R. Mercader, O. E. Piro, *J. Phys. Chem. Solids* **1986**, *47*, 239.
[19] C. N. Dibenedetto, T. Sibillano, R. Brescia, M. Prato, L. Triggiani, C. Giannini, A. Panniello, M. Corricelli, R. Comparelli, C. Ingrosso, N. Depalo, A. Agostiano, M. L. Curri, M. Striccoli, E. Fanizza, *Molecules* **2020**, *25*, 2939.
[20] A. Abbas, E. Oswald, J. Romer, A. Lenzer, M. Heiland, C. Streb, C. Kranz, A. Pannwitz, *Chem. -Eur. J.* **2023**, *29*, e202302284.
[21] U. Baxa, in *Methods In Molecular Biology*, Vol. *1682*, Humana Press, New York, NY **2018**.
[22] L. S. Hirst, A. Ossowski, M. Fraser, J. Geng, J. V. Selinger, R. L. B. Selinger, *Proc. Natl. Acad. Sci. USA* **2013**, *110*, 3242.
[23] E. A. Medlycott, G. S. Hanan, *Chem. Soc. Rev.* **2005**, *34*, 133.
[24] S. A. McFarland, D. Magde, N. S. Finney, *Inorg. Chem.* **2005**, *44*, 4066.
[25] P. Innocenzi, H. Kozuka, T. Yoko, *J. Phys. Chem. B* **1997**, *101*, 2285.
[26] K. Mori, M. Kawashima, K. Kagohara, H. Yamashita, *J. Phys. Chem. C* **2008**, *112*, 19449.
[27] D. Wencel, C. Dolan, M. Barczak, T. E. Keyes, C. McDonagh, *Nanotechnology* **2013**, *24*, 365705.
[28] J. Hjort Ipsen, G. Karlström, O. G. Mourtisen, H. Wennerström, M. J. Zuckermann, *Biochim. Biophys. Acta* **1987**, *905*, 162.
[29] S. M. N. Uddin, S. Laokroekkiat, Md. A. Rashed, S. Mizuno, K. Ono, M. Ishizaki, K. Kanaizuka, M. Kurihara, Y. Nagao, T. Hamada, *Chem. Commun.* **2020**, *56*, 1046.
[30] L. A. Bagatolli, in *Reviews in Fluorescence*, Springer, New York, NY **2007**.
[31] A.-L. Robson, P. C. Dastoor, J. Flynn, W. Palmer, A. Martin, D. W. Smith, A. Woldu, S. Hua, *Front. Pharmacol.* **2018**, *9*, 80.
[32] E. Mamontova, J. Long, R. A. S. Ferreira, A. M. P. Botas, F. Salles, Y. Guari, L. D. Carlos, J. Larionova, *Nanoscale* **2019**, *11*, 7097.
[33] X. Han, W.-W. He, T. Zhou, S. Ma, *Inorg. Chem. Front.* **2024**, *11*, 3707.
[34] E. J. Canto-Aguilar, M. A. Oliver-Tolentino, G. Ramos-Sánchez, I. González, *Electrochim. Acta* **2021**, *371*, 137828.
[35] S. S. Kaye, J. R. Long, *J. Am. Chem. Soc.* **2005**, *127*, 6506.
[36] M. Pyrasch, A. Toutianoush, W. Jin, J. Schnepf, B. Tieke, *Chem. Mater.* **2003**, *15*, 245.
[37] R. S. Khnayzer, B. S. Olaiya, K. A. El Roz, F. N. Castellano, *ChemPlusChem* **2016**, *81*, 1016.
[38] A. Vaidyalingam, P. K. Dutta, *Anal. Chem.* **2000**, *72*, 5219.
[39] D. M. Klein, S. Rodríguez-Jiménez, M. E. Hoefnagel, A. Pannwitz, A. Prabhakaran, M. A. Siegler, T. E. Keyes, E. Reisner, A. M. Brouwer, S. Bonnet, *Chem. - Eur. J.* **2021**, *27*, 17203.
[40] S. Troppmann, E. Brandes, H. Motschmann, F. Li, M. Wang, L. Sun, B. König, *Eur. J. Inorg. Chem.* **2016**, *2016*, 554.
[41] S. Troppmann, B. König, *ChemistrySelect* **2016**, *1*, 1405.
[42] S. Mabrey, J. M. Sturtevant, *Proc. Natl. Acad. Sci. USA* **1976**, *73*, 3862.
[43] F. A. Heberle, G. W. Feigenson, *Cold Spring Harbor Perspect. Biol.* **2011**, *3*, a004630.
[44] S. A. Irfan, R. Razali, K. KuShaari, N. Mansor, B. Azeem, A. N. F. Versypt, *J. Controlled Release* **2018**, *271*, 45.
[45] J. M. May, Z. Qu, R. R. Whitesell, *Biochim. Biophys. Acta* **1995**, *1238*, 127.
[46] V. Kumaravel, M. Imam, A. Badreldin, R. Chava, J. Do, M. Kang, A. Abdel-Wahab, *Catalysts* **2019**, *9*, 276.
[47] M. Wang, S. Shen, L. Li, Z. Tang, J. Yang, *J. Mater. Sci.* **2017**, *52*, 5155.
[48] D. M. Klein, L. Passerini, M. Huber, S. Bonnet, *ChemCatChem* **2022**, *14*, e202200484.
[49] M. H. Gehlen, *J. Photochem. Photobiol. C* **2020**, *42*, 100338.
[50] A. S. Tanwar, R. Parui, R. Garai, M. A. Chanu, P. K. Iyer, *ACS Meas. Sci. Au* **2022**, *2*, 23.
[51] R. Ballardini, M. T. Gandolfi, V. Balzani, *Inorg. Chem.* **1987**, *26*, 862.
[52] B. R. Lentz, D. A. Barrow, M. Hoechli, *Biochemistry* **1980**, *19*, 1943.
[53] L. Hu, P. Zhang, Q. Chen, N. Yan, J. Mei, *Dalton Trans.* **2011**, *40*, 5557.
[54] P. Nie, L. Shen, H. Luo, B. Ding, G. Xu, J. Wang, X. Zhang, *J. Mater. Chem. A* **2014**, *2*, 5852.
[55] M. Ishizaki, K. Kanaizuka, M. Abe, Y. Hoshi, M. Sakamoto, T. Kawamoto, H. Tanaka, M. Kurihara, *Green Chem.* **2012**, *14*, 1537.
[56] A. Gotoh, H. Uchida, M. Ishizaki, T. Satoh, S. Kaga, S. Okamoto, M. Ohta, M. Sakamoto, T. Kawamoto, H. Tanaka, M. Tokumoto, S. Hara, H. Shiozaki, M. Yamada, M. Miyake, M. Kurihara, *Nanotechnology* **2007**, *18*, 345609.